University of Nevada, Reno

Numerical Investigation of Magnetically Driven Isentropic Compression of Solid Aluminum Cylinders with a Semi-Analytical Code

A thesis submitted in partial fulfillment of the requirements for the degree of Master of Science in Physics

By

Billy T. Largent

Dr. Hiroshi Sawada / Thesis Advisor

May, 2017

THE GRADUATE SCHOOL

We recommend that the thesis
prepared under our supervision by

BILLY T. LARGENT

Entitled

Numerical Investigation Of Magnetically Driven Isentropic Compression Of Solid Aluminum Cylinders With A Semi-Analytical Code

be accepted in partial fulfillment of the
requirements for the degree of

MASTER OF SCIENCE

Hiroshi Sawada, Ph.D., Advisor

Alla S. Safronova, Ph.D., Committee Member

David M. Leitner, Ph.D., Graduate School Representative

David W. Zeh, Ph.D., Dean, Graduate School

May, 2017

ABSTRACT

The state of matter at extremely high pressures and densities is of fundamental interest to many branches of research, including planetary science, material science, condensed matter physics, and plasma physics. Matter with pressures, or energy densities, above 1 megabar (100 gigapascal) are defined as High Energy Density (HED) plasmas. They are directly relevant to the interiors of planets such as Earth and Jupiter and to the dense fuels in Inertial Confinement Fusion (ICF) experiments. To create HEDP conditions in laboratories, a sample may be compressed by a smoothly varying pressure ramp with minimal temperature increase, following the isentropic thermodynamic process. Isentropic compression of aluminum targets has been done using magnetic pressure produced by megaampere, pulsed power currents having ~ 100 ns rise times.

In this research project, magnetically driven, cylindrical isentropic compression has been numerically studied. In cylindrical geometry, material compression and pressure become higher than in planar geometry due to geometrical effects. Based on a semi-analytical model for the Magnetized Liner Inertial Fusion (MagLIF) concept, a code called “SA” was written to design cylindrical compression experiments on the 1.0 MA Zebra pulsed power generator at the Nevada Terawatt Facility (NTF). To test the physics models in the code, temporal progresses of rod compression and pressure were calculated with SA and compared with 1-D magnetohydrodynamic (MHD) codes. The MHD codes incorporated SESAME tables, for equation of state and resistivity, or the classical Spitzer model. A series of simulations were also run to find optimum rod diameters for 1.0 MA and 1.8 MA Zebra current pulses. For a 1.0 MA current peak and 95 ns rise time, a maximum compression of ~ 2.35 (~ 6.3 g/cm^3) and a pressure of ~ 900 GPa within a 100

μm radius were found for an initial diameter of 1.05 mm. For 1.8 MA peak simulations with the same rise time, the initial diameter of 1.3 mm was optimal with ~ 3.32 (~ 9.0 g/cm^3) compression.

ACKNOWLEDGEMENTS

I would like to thank Prof. Hiroshi Sawada who patiently guided me throughout the research process, revised and contributed to the thesis manuscript, and provided moral support. This work would not have been completed without his help.

I would like to thank the committee members Prof. Alla Safronova, Prof. David Leitner, and Prof. Jonathan Weinstein for reviewing this thesis, attending the defense, and providing thoughtful commentary.

Thanks also goes to Prof. Bernhard Bach and Prof. Radu Presura who helped support my graduate school career through assistantships and student work.

Lastly, I thank all others who helped me in any way throughout my academic career.

Table of Contents

List of Tables

List of Figures

I. COMPRESSION OF MATERIALS TO EXTREME PRESSURES

A. Introduction

Knowledge of material properties under extremely high pressures is fundamental for planetary physics, material science, condensed matter physics, and plasma physics. A research area on materials with pressure, or energy density, above 1 Mbar (10^{11} J/cm^3 or 100 GPa) is known as "High Energy Density Physics" (HEDP). This high-energy density (HED) state of matter does not exist naturally on Earth but knowledge has grown rapidly from laboratory astrophysics and inertial confinement fusion (ICF) work. In experiments ranging from small-scale apparatus at universities to large-scale facilities at national laboratories, HED conditions are typically attained using a diamond anvil cell (DAC) for static compression or by shock waves created through radiation or pulsed current for dynamic compression. In static compression, external pressure is a single impulse or perturbation that does not change over experimental time scales and the target itself does not move. The diamond anvil cell may use two equally large diamonds and an external mechanism, such as a piston, to compress the target together [1]. Although DAC allows precise control of pressure for material property measurements in the static state, the highest accessible pressure domain is limited to ~ 100 - 200 GPa for low temperatures. An example of a piston-based DAC is FIG. 1 below [2].

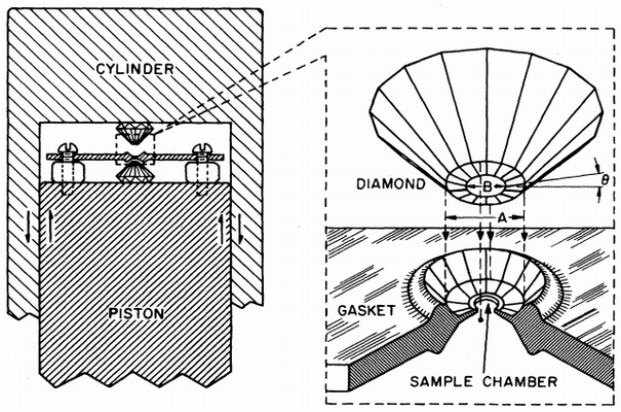

FIG. 1. A piston-based diamond anvil cell experimental setup capable of 100 GPa or larger pressures within the target [2].

In dynamic compression, the external force evolves over time and the target moves with kinetic properties altered. Examples include flyer plate impacts, magnetic pressure provided by a current pulse, and ablation driven shock waves due to lasers or an x-ray bath. At Sandia National Laboratory (SNL), a magnetically accelerated flyer plate impacted a planar aluminum drive plate, compressing it to ~ 500 GPa [3]. A diagram of the experiment is below in FIG. 2. In inertial confinement fusion (ICF) implosions, a spherical shell filled with deuterium-tritium fuel is compressed by laser or x-ray radiation driven shock waves. The stagnating core pressure may reach 1 Gbar (100 TPa) [4], [5].

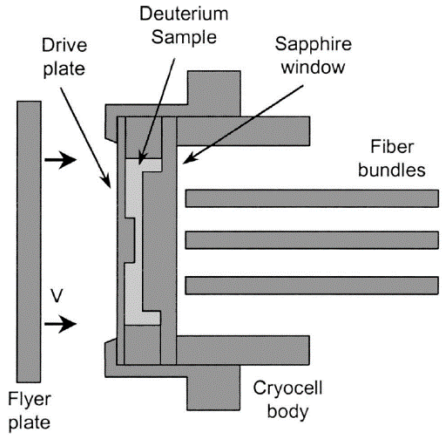

FIG. 2. An example of a flyer plate-based compression experiment. The plates hit the aluminum drive plate, bringing it up to as high as 500 GPa. The drive plate then performs work on the Li-D sample, the actual final target [3].

Material compression by strong shock waves is an irreversible adiabatic process that increases the target entropy and temperature as density increases. Excessive heat in the rapid compression melts and breaks the lattice structures. As an alternative, a gradually increasing pressure load has been used to isentropically compress a material. Experiments performed using the 26 MA Z pulsed power accelerator at Sandia National Laboratory (SNL) utilized a carefully shaped current pulse to achieve isentropic compression of a planar aluminum sample to 240 GPa [6], [7]. In addition, ramp compression experiments using the high-power lasers of the National Ignition Facility (NIF) at Lawrence Livermore National Laboratory (LLNL) produced pressures in the range of 330 GPa in tantalum [8]. Although demand for experimental data of materials at high energy density conditions is high, the shot rates are extremely limited with ~ 3 shots per week at Z and 1 shot per day at NIF. To accelerate exploration of solid material properties such as equation of state, conductivity, opacity, and lattice structures in the HED range, it is necessary to study compression techniques that allow a higher data acquisition rate.

The research presented here is motivated by development of magnetically driven, cylindrical isentropic compression capability at the Nevada Terawatt Facility (NTF) using the 1.0 MA Zebra pulsed power machine. As demonstrated in planar and cylindrical isentropic compression experiments at SNL, a slow ramp current produced by a pulsed power system can compress matter isentropically [6], [9]. By using a strong current pulse running on the surface and within a solid metal cylinder, isentropic compression can be achieved by magnetic pressure along with geometrical compression by the converging compression waves. With this scheme, peak pressure of the target metal rod may reach 300 GPa with a university-scale machine. The primary objective of

our research is to develop a semi-analytical numerical code for designing a metal rod compression experiment using pulsed power. The simulation results were first compared to outcomes from using magnetohydrodynamic (MHD) codes. Then, using our code, compression of solid aluminum rods with various diameters from 0.6 to 3.0 mm was studied for 1.0 MA and 1.8 MA, 95 ns rise time, Zebra-style current pulses.

B. Shock and Isentropic Compression

Rapid compression can form shock waves. A shock wave is treated in thermodynamics as an irreversible adiabatic process with jump discontinuities in both intensive and extensive variables, such as temperature and entropy. The shock wave obeys the thermodynamic Rankine-Hugoniot relation and discontinuities get larger with higher speed and stronger shocks. Weaker types of shock processes are typically multiple impulse and have waves at or above the target material's sound speed. FIG. 3 below is a pressure-volume (PV) diagram and illustrates changes of material state by a single strong shock wave, multiple weak shock waves, and an ideal, reversible adiabatic process. The ideal strong shock "Hugoniot" curve is the steepest and fastest. The material will experience large discontinuities during the process. The "multiple shock" curve is for sequential weak shocks with smaller discontinuities. Density may be increased to a higher magnitude than for the strong shocks since max compression may be fixed for the high external pressure limit. The "adiabat" curve is an ideal, reversible adiabat. It is an isentrope [10, pp. 62-67] [11].

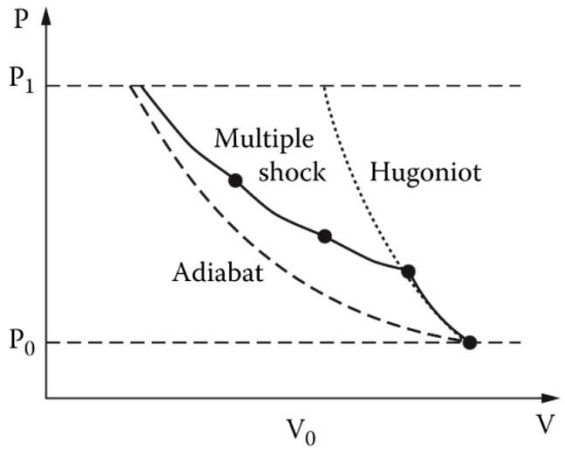

FIG. 3. Illustration of shock adiabatic curves. Typically, weak shocks are in succession while strong shocks are a single main thrust [10, p. 66].

The entropy of a thermodynamic system is considered a measure of the "disorder" of the system. It is quantified as the natural log of system multiplicity, or the number of possible states, multiplied by the Boltzmann constant

$$S = k_B \ln \Omega. \quad (1)$$

The second law of thermodynamics treats entropy growth as an irreversible result of all processes. It is proportional to the change in system energy and given by

$$dS = \frac{dU}{T}. \quad (2)$$

In an isentropic compression, system entropy is meant to stay constant and the entire process is reversible. This compression is discussed in two forms, the textbook ideal case and the quasi-isentropic case achieved in lab and often referred to as just "isentropic".

In the ideal case, compression is both adiabatic and reversible. It is also not isothermal. No heat is added to or lost by the system and the energy increase due to work could be used to return the system to initial conditions. There are no dissipative effects such as friction. An example would be a completely insulated piston compression with no friction on the walls and no routes from the walls to the outside allowing heat to escape. After piston release and target expansion, it would be impossible to distinguish if compression occurred because entropy did not increase.

Quasi-isentropic compression is reversible but not adiabatic. If the piston compression example had walls with friction and was connected to the outside world, energy would be lost by the system due to overcoming friction. The situation is still reversible since the compressible object may return to its original form after release and, locally, entropy would be the same. Universally, entropy would increase due to lost heat from the system.

Ideally, quasi-isentropic compression maintains the temperature of the target. Extra energy gained by the compressed object is lost to friction, radiation, and other dissipative processes at the same rate it is gained from the piston work. Therefore, the object does not change temperature. To attempt this, the compression force must be smooth and slow to prevent excess energy and shocks. Since it is thermodynamically impossible to prevent at least some warming, the quasi-isentropic process is the lower limit for laboratory compression that minimizes heat.

C. Motivations for Aluminum Isentropic Compression Research

Solid aluminum at room temperature has the lattice structure of face-centered cubic (FCC). At high pressures, FCC structure shifts to the hexagonal close-packed (HCP) state. Experimental pressure and temperature conditions must be simultaneously above ~ 220 GPa and below ~ 6000 K respectively [12]. FIG. 4 below shows a pressure-temperature (PT) diagram for aluminum with thermodynamic curves representing strong and weak shock processes as well as isentropic compression. A single ideal strong shock follows the Hugoniot curve. Stronger shocks may allow the pressure of the aluminum target to be high but temperature rapidly increases beyond the melt line and causes the loss of solid state. Using multiple shock waves pressure can be increased without excessive temperature ramp but this approach prevents material conditions from reaching the highest pressure and lowest temperature regimes. Isentropic compression of aluminum maintains the temperature well below the melt line while keeping high pressure even to 400 GPa. Theory predicts another phase transition from HCP to body-centered cubic (BCC) occurring at ~ 350 to 380 GPa but this has not been experimentally confirmed [13]**.**

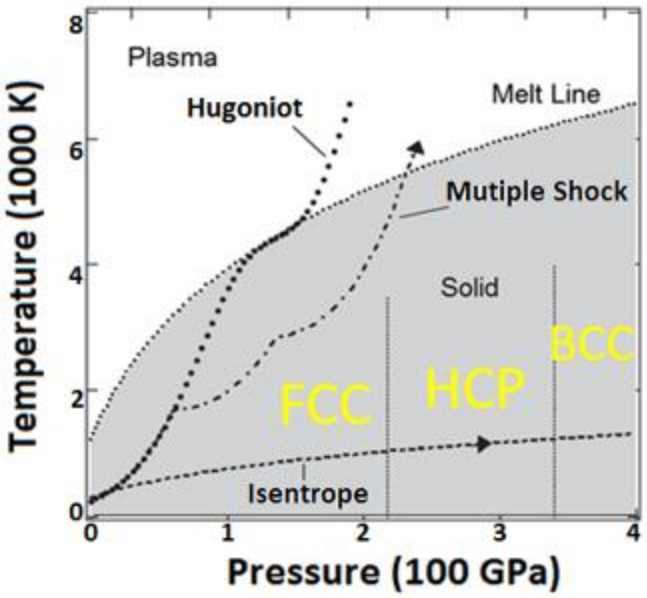

FIG. 4. PT diagram with strong shock Hugioniot and a possible weak shock curve process reaching above the melt line. Isentrope has least possible temperature growth [13].

II. PAST EXPERIMENTAL WORK IN ISENTROPIC COMPRESSION

A. Planar Isentropic Compression

At present day facilities, isentropic compression experiments have been conducted using laser driven plasma loads, direct laser driven ablation, and current driven, magnetic compression in planar target geometries [6], [7], [13], [14]. In planar geometry, pressure comes in only from one side. The Velocity Interferometer System for Any Reflector (VISAR) diagnostic can be used to find velocities within target material. As an example, FIG. 5 below diagrams the "plasma reservoir driven" experiment at the University of Rochester's Laboratory for Laser Energetics (LLE). In this experiment, a polyimide ablator was irradiated by 10 OMEGA lasers at ultra-violet wavelengths to create a strong shock wave in a polystyrene reservoir. As the shock wave traveled through the plastic and exited, low density and low ionization plasma were released into a vacuum gap. The plasma then behaved as a piston, isentropically compressing the final target, a 6061-T6 Al foil. VISAR probing of the target was through a lithium-fluoride window by a visible 532 nm laser. Velocity measurements were made by counting fringe shifts created by phase shifted laser light reflected from the compression wave. When velocity information was paired with a known equation of state and simulations, these measurements allowed determination of material pressure within the target. The interferometry would also suggest shock wave occurrence if sharp distortions in fringe lines were seen [13]. In FIG. 6 below, sample VISAR fringe lines are shown as well as pressure and velocity data derived from the diagnostic. In the experiment, the ablator was irradiated with a combined ~ 2 kJ at a peak intensity of ~ 8×10^{13} W/m^2 so that a 10 μm Al foil could be compressed by the ensuing plasma. Utilizing an aluminum equation of state database,

operative up to ~ 300 GPa, particle and shock velocities were analyzed. A result of ~ 200 GPa and a compression of 2 were found [13].

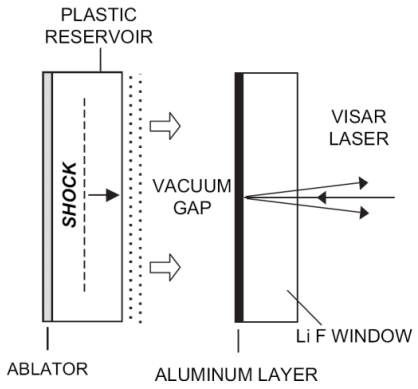

FIG. 5. "Plasma reservoir driven" experiment at the University of Rochester LLE [13].

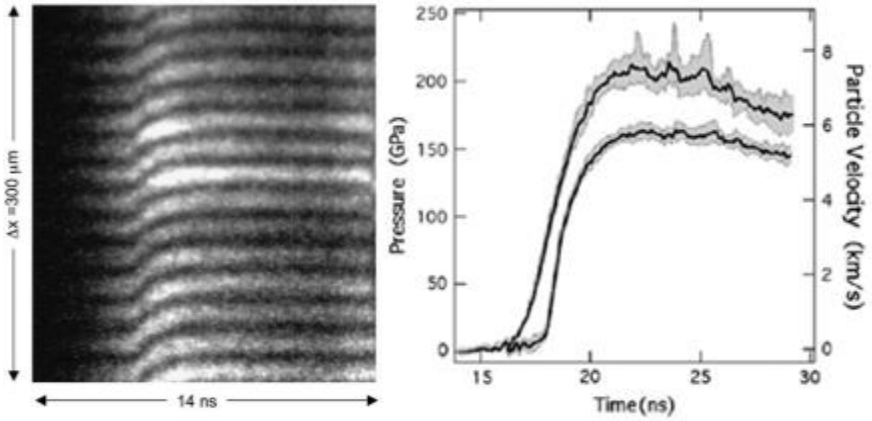

FIG. 6. VISAR example using a CCD image created by 532 nm laser. Horizontal axis is time. Fringe shift represents a 5.39 km/s shift. The lower curve is for velocity while the upper curve is for pressure [13].

Direct laser ablation has been successful using a long, smooth pulse form, or “ramped laser irradiance.” FIG. 7 shows the laser pulse shape as well as an experimental diagram. The TRIDENT laser at Los Alamos National Laboratory (LANL) ablated a silicon target with defocused light. A “loading wave” was formed without an ablator. The 2.5 ns laser pulse delivered ~ 62 J with the frequency doubled to 527 nm. A VISAR system reflected off the compressed target from the other side and measured a result of 15 GPa in both 30 and 59 μm thick silicon [14].

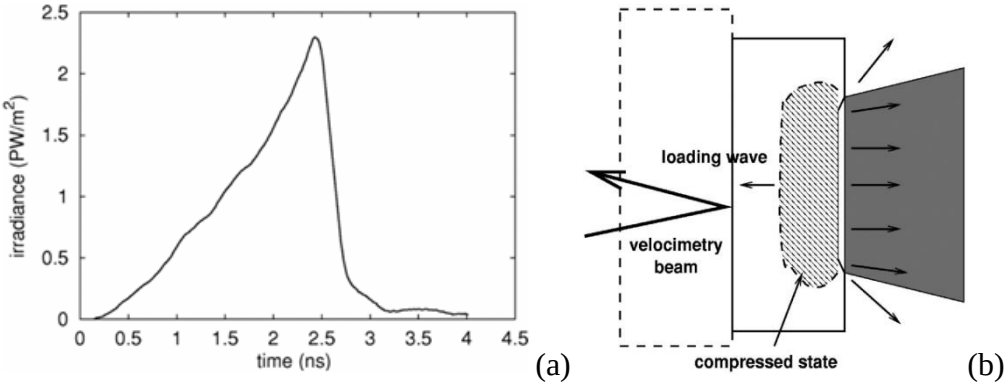

FIG. 7. (a) Long, smooth laser intensity curve (b) Isentropic compression experimental diagram [14].

Another route to isentropic compression is through magnetic pressure created by a pulsed power generator. This type of generator may deliver megaampere peak currents within an extremely short pulse rise time via the discharge of Marx capacitor banks. Multi-tesla magnetic fields and > 100 GPa magnetic pressures are possible. Two examples of such generators are the 200 kJ, 1.0 MA peak Zebra machine at the Nevada Terawatt Facility and the 21 MJ, 26 MA peak Z at Sandia National Laboratory [15], [16], [17], [18]. In FIG. 8, an isentropic compression experiment with a planar target at Sandia National Laboratory's Z is diagrammed. In the experiment, a short circuit type configuration was used. Current density traveled on the cathode plate and created a magnetic field within the vacuum gap. As current density moved onto the anode, the azimuthally directed magnetic field interacted with the current and created pressure on the target highlighted in green. A VISAR system measured a pressure of 240 GPa within the 6061-T6 Al target [6], [7].

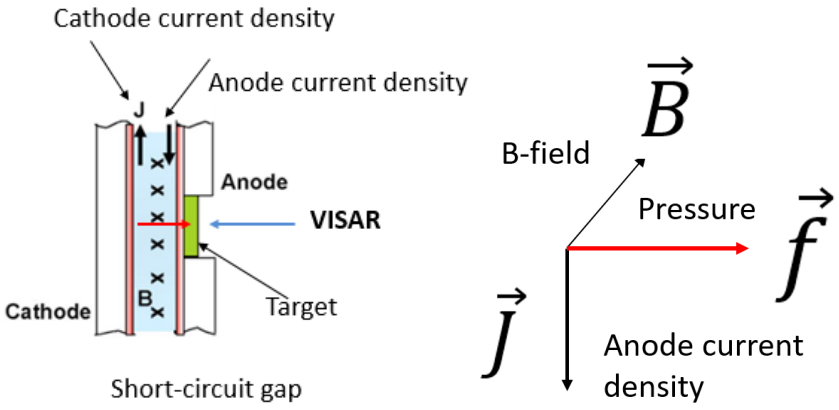

FIG. 8. Z compression experiment diagram showing the short circuit load providing the J x B force onto the highlighted target [19].

B. Cylindrical Isentropic Compression by Magnetic Field Pressure

Ampere's Law for magnetostatics states that

$$\nabla \times \vec{\mathbf{B}} = \mu_0 \vec{\mathbf{J}}. \quad (3)$$

Where $\vec{\mathbf{B}}$ is the magnetic field, in teslas, provided by the current density $\vec{\mathbf{J}}$ in units of amperes per square meter. For the case of a uniform rod of current, we have for the magnetic field at the solid rod surface and outside

$$\mathrm{B} = \frac{\mu_0 \mathrm{I}}{2\pi \mathrm{r}}. \quad (4)$$

Here, I is the current in amperes, r is the distance from the rod center axis in meters, and μ_0 is the vacuum permeability constant in SI units. Within the solid rod, the solution is

$$\mathrm{B} = \frac{\mu_0 \mathrm{I r}}{2\pi \mathrm{r}_{\mathrm{rod}}^2}, \quad (5)$$

where $\mathrm{r} < \mathrm{r}_{\mathrm{rod}}$. The magnetic field pressure provided by the uniform current is

$$\mathrm{P}_{\mathrm{mag}} = \frac{\mathrm{B}^2}{2\mu_0}. \quad (6)$$

For a constant 1.0 MA current and a uniform rod of current with a diameter of 1 mm, eqs. (5) and (6) yield a magnetic field of ~ 400 tesla and a magnetic pressure of 63.7 GPa at the surface.

For a solid cylinder the problem geometry is shown in FIG. 9 below. Current density is directed downward along the surface of, and within, the rod. The magnetic field is oriented clockwise and is tangential to the surface normal of the rod. The magnetic field pressure is pointed inward towards the rod center axis. As the target is compressed, $\mathrm{r}_{\mathrm{rod}}$ gets smaller and the magnetic field within gets stronger in space. This strengthens the spatially decaying magnetic pressure inside.

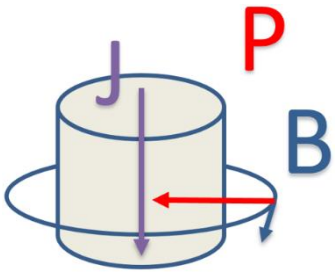

FIG. 9. Magnetic pressure, compression from magnetic field created by current.

Cylindrical geometry allows compression of the target not only through magnetic pressure itself but also in the form of coalescence of compression waves. This is referred to as geometrical compression. If cylinder targets are used, higher domains of density, temperature, and pressure may be achieved using university-scale pulsed power generators.

Cylindrical compression has other advantages. If the cylinder surface is uniform, being machined out of one material piece, magnetic pressure may be isotropic and lead to isotropic, uniform compression of the target. For magnetohydrodynamic instabilities, 2-D geometry is more stable than 3-D. Also, hydrodynamic instabilities may remain on the surface so that interior regions of interest for equations of state, phase shifts, and other topics would be unaffected [20], [21].

The primary difficulty of cylindrical targets is a blocked line of sight due to high material and electron densities. Planar targets allow shadowgraphy, interferometry, and VISAR to obtain material densities and velocities. For a cylindrical compression in which material is driven inward it is not possible to get a reflection and an uncorrupted record as if through a window. Also, if unprecedented pressures are reached, no equation of state data may be available for velocity matching.

To resolve these difficulties, x-ray diagnostics may be used. A backlighter is created by hitting foils placed near the compression experiment with a high intensity laser. Electrons energized by the laser emit bremsstrahlung, or "braking radiation," as they interact with foil ions [22]. This process provides high frequency radiation that can image compression target interiors and allow material density to be found via imaging plates and filtering. X-ray bursts provided by pulsed power driven x-pinches may also perform this role [23]. X-ray diffraction allows for pressures to be derived from lattice spacing [24]. This diagnostic has been used to observe phase state changes in iron [25]. Compton scattering has been able to obtain radiographs of the interiors of compression targets [26]. Lastly, x-ray Thompson scattering may allow the acquisition of electron temperature and ionization data [27].

C. Cylindrical Isentropic Compression Experiments

Cylindrical isentropic experiments have been conducted with high explosives and pulsed power generators. High explosives have been used in different experimental apparatus designs and on different targets, such as deuterium or liquid xenon [28], [29], [30], [31], [32].

FIG. 10 shows a setup for a HE experiment attempting to compress hydrogen and deuterium gases to warm dense matter with non-ideal properties. The purpose was to study strongly coupled plasma [28]. X-ray radiographic images of the compressed matter were captured with hard x-rays from a betatron source [33]. A 20% increase in the mass density of the compressed matter was successfully deduced and compared with MHD simulations [28].

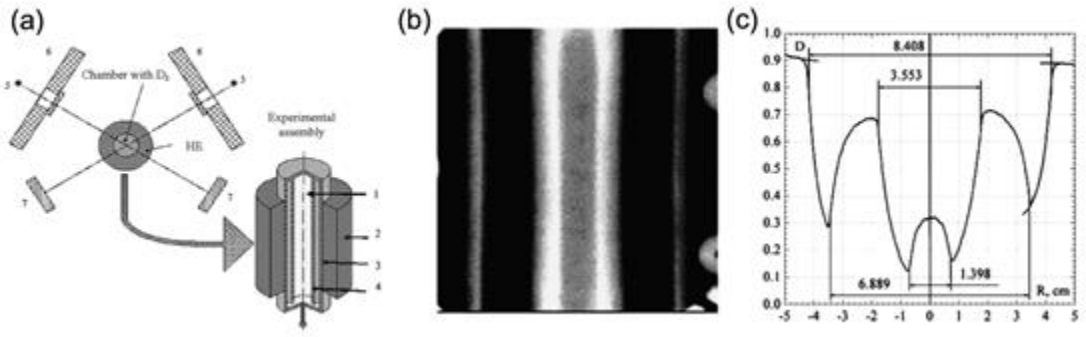

FIG. 10. (a) High explosive isentropic compression experiment diagram (b) x-ray radiographic image of target interior after compression (c) lineout showing density profile [28].

Experiments have also been conducted with pulsed power generators primarily to research implosion dynamics, instabilities, and surface plasma formation due to the high current [9], [21], [34], [35]. Compression of a solid cylinder of Be with SNL's Z reached ~ 550 GPa with ~ 3 compression. This was diagnosed by use of x-ray backlighting, simulation, and surface fitting [9].

D. Study of Surface Plasma Formation on Compressed Solid Cylinders at the Nevada Terawatt Facility

To examine the conditions of plasma creation on conductive metal surfaces, aluminum cylinders were driven with high current at the Nevada Terawatt Facility (NTF). The Zebra pulsed power generator delivered a ~ 1.0 MA peak current and ~ 100 rise time. 6061-T6 Al rods were varied from 0.5 mm to 2 mm in initial diameter with ~ 1 cm of height. Plasma was created once the magnetic field reached 220 tesla within aluminum vapor formed through ohmic heating [34]. Decreasing rod diameter reduced the time needed for plasma to be created and increased surface temperatures. A distinguishing feature of the experiment was the use of tighter fitting "knife edge" hardware, "barbell" and "hourglass" loads. These loads are shown in FIG. 11. The hardware was placed within the Zebra chamber. The "hourglass" load makes the anode, cathode, and target rod all one piece. This prevents non-thermal plasma creation caused by target rod exposure to hardware electrical contacts and arcing. While the barbell type is not all one piece and does leave the rod open to contact, the distances are greater than for typical loads. These specialized loads have the benefit of making the plasma creation timing predictable [36].

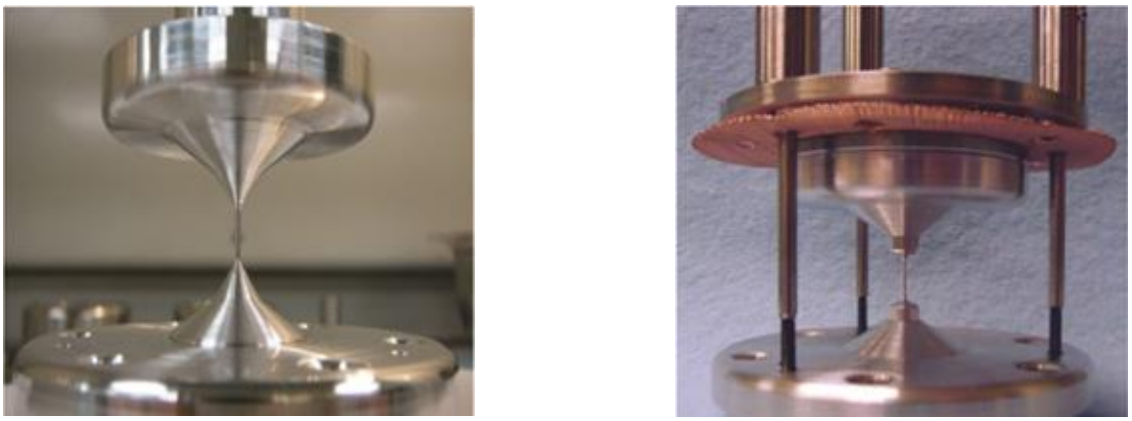

FIG. 11. "Hourglass" and "barbell" load types deployed on Zebra pulsed power generator at the NTF [36].

Hydrodynamic instabilities remained near the surface during the current pulse rise and were dependent on initial rod diameter. As shown by FIG. 12, the skinnier rod of 0.5 mm diameter had instabilities at 583 kA while for 1.0 mm diameter no noticeable instabilities appeared near the end of the pulse rise time at 903 kA [20].

(a) (b)

FIG. 12. ICCD imaging of cylindrical compression target at the NTF, showing lack of penetration of instabilities into interior for (a) 0.5 mm initial diameter at 583 kA (b) 1 mm initial diameter at 903 kA [20].

A shadowgraph is an image of experimental material captured by shining a laser through the target onto a charge-coupled device (CCD), or digital camera. Dark regions of high density are shown if the laser is not above the plasma frequency of the material. In FIG. 13 below, shadowgraphs show unstable surface plasma expansion from the original diameter (the segmented line) for a 0.8 mm diameter experiment. In contrast, expansion was much smaller for 2.0 mm diameter. These images cannot help in diagnosing interior regions where the plasma frequency is higher [35].

FIG. 13. Turbulent surface plasma on cylindrical liner target, for 0.8 mm diameter, and little plasma for 2.0 mm diameter near current peak time [35].

To estimate the plasma surface temperatures, visible light radiometry was used based on filtered greenlight, black body emission captured by photodiodes. For the 2 mm diameter rod, the wider diameter prevented generation of strong magnetic fields. The surface temperature only reached 0.7 eV at current peak. For the skinnier 0.5 mm diameter rod, plasma spectra were detected and temperatures reached 20 eV at current peak time [35].

III. SEMI-ANALYTICAL CODE DESIGN

We now discuss a semi-analytical code we have created to simulate cylindrical isentropic compression of metal rods using the 1.0 MA Zebra pulsed power generator at the Nevada Terawatt Facility. The code, called SA, was developed based on a semi-analytical model for the Magnetized Liner Inertial Fusion (MagLIF) concept [37].

Past simulation work has required use of much processing time or of commercial or user-restricted codes. This prohibits experimentalists and students from quickly exploring an experiment's parameter space to solve design issues, such as finding ideal rod diameters and diagnostic activation times. It is also currently unknown what the parameter spaces are for isentropic compression in solid aluminum cylinders at high pressures. The creation of SA allows us to analyze baseline target geometry and possible experimental results for isentropic compression experiments on Zebra.

A. A Semi-Analytical Model for MagLIF

Recently, McBride and Slutz created and published a 1-D semi-analytical model for the MagLIF concept [37]. FIG. 14 below shows a diagram of the MagLIF approach. A thin metal cylinder, or liner, containing deuterium-tritium fusion fuel is compressed by an azimuthal magnetic field generated by high currents flowing down the liner. Before the current pulse, an axial magnetic field created by separate nearby coils is applied to magnetize the fuel and a green, high power, 5 - 10 kJ laser heats the fuel to 100 - 500 eV. Azimuthal compression strengthens the axial field and can contain the radiating, charged alpha particles released by fusion reactions necessary for high gain [38].

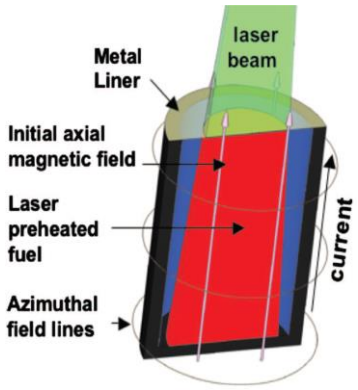

FIG. 14. Diagram of MagLIF concept [37]

The concept of MagLIF was numerically tested first by the classified 2-D radiation magnetohydrodynamic code LASNEX [38]. The initial MagLIF experiments were conducted on Z at Sandia National Laboratory in a 19 MA current peak, ~ 125 ns rise time configuration [39]. Afterwards, the previously mentioned semi-analytical model was developed based on experimental results [37]. Investigation of the physics involved in MagLIF, such as interaction of the pre-heat laser with the target window, is currently ongoing [39].

The semi-analytical model was designed for computationally lighter simulations. Equations of motion were reduced to 1^{st} and 2^{nd} order ordinary differential equations in time. Material and magnetic field pressure calculations were simplified and incorporated numerical constants based on matching experimental results [37].

B. Model Features Necessary for Compression of Solid Cylinders

To simulate solid cylinder compression, we modified the semi-analytical model and "filled in" the hollow interior. For our purposes, only equations of motion, magnetic and material pressures, ohmic heating, and simple radiation physics are needed.

In SA, the radial space of the target cylinder is divided into discrete 1-D spaces called shells. Each shell has its own density, thermal energy, and internal material pressures with no heat conduction or transportation between. On both sides of the shell are interfaces, designated as $r_{l,i}$, and there are interfaces separating the liner from the inner "boundary" and outer vacuum. These are r_g and r_l respectively. Each interface has an equation of motion containing pressure terms for both sides [37]. These are given by the following equations

$$\ddot{r}_{l,i} = \frac{p_{l,s=i-1} - p_{l,s=i}}{m_{ls}} \cdot 2\pi r_{l,i} \cdot h, \tag{7}$$

$$\ddot{r}_{l} = \frac{p_{l,s=N_{ls}} - p_{B_{\theta lv}} - p_{\bar{B}_{zv}}}{m_{ls}/2} \cdot 2\pi r_{l} \cdot h, \tag{8}$$

and

$$\ddot{r}_{g} = \frac{p_{g} + p_{\bar{B}_{zg}} - p_{l,s=1}}{m_{ls}/2} \cdot 2\pi r_{g} \cdot h. \tag{9}$$

$p_{l,s=i}$ is the pressure sum of the ith shell, including material pressure, magnetic pressure at interface location, and artificial viscosity. $r_{l,i}$ is the radial location of the ith interface. h is the shell height. $p_{B_{\theta lv}}$ is the magnetic pressure at the liner surface. $p_{\bar{B}_{zv}}$ is the pressure due to the average axial magnetic field in the vacuum region and $p_{\bar{B}_{zg}}$ is the pressure from average axial magnetic field in the gas region. Neither are included for solid cylindrical compression since no axial field is present. p_g is the fuel pressure, again not

used for a solid cylinder. $p_{l,s=1}$ is the pressure from the innermost shell. m_{ls} is the mass of a shell. r_l is the outermost interface location and r_g is the innermost interface location. In the model, all units are SI and not normalized [37].

In FIG. 15, the different internal interfaces are represented by the segmented lines, with the innermost interface, r_g, and the outermost interface, r_l, as solid lines. The magnetic field solution is also shown.

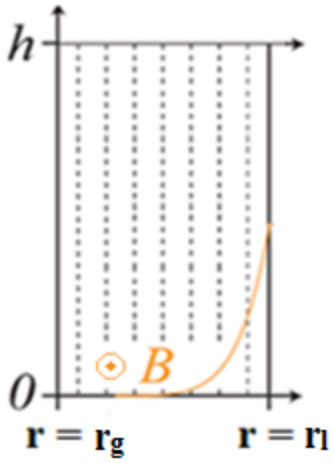

FIG. 15. Illustration of liner shells with interfaces and internal magnetic field [37]. In the actual simulation, not all shells are evenly spaced to avoid code failure.

For numerical solving, magnetic field decay is adapted into a simple ratio or proportion based on the liner width [37]. This approximation is partially justified because the target radius is assumed wider than skin depth. The strengths of the magnetic field and magnetic pressure at the ith interface are given as

$$B_i = \frac{\mu_0 I_l}{2\pi r_l}\left(\frac{r_i - r_1}{r_l - r_1}\right)^{\beta}, \tag{10}$$

and

$$P_{magnetic,i} = \frac{B_i^2}{2\mu_0} = \frac{\mu_0 I^2}{8\pi^2 r_i^2}, \tag{11}$$

where I is the time-dependent current. The constant β, determined by the resistivity, skin depth δ_{skin}, and the liner thickness at simulation start, is given by

$$\beta = \left\{\left|\frac{\ln(1/e)}{\ln\left(\frac{\delta_{l0}-\delta_{skin}}{\delta_{l0}}\right)}\right|\right\}, \tag{12}$$

and

$$\delta_{skin} = \sqrt{\frac{4\rho_e\tau_r}{\pi\mu_0}}, \tag{13}$$

where ρ_e is "initial electrical resistivity" of the target, τ_r is "rise time" of the current pulse, and δ_{l0} is the "initial thickness of the liner" [37].

Material pressure, uniform within each shell, is a sum of ideal gas, "cold" material, and artificial viscosity terms. The combined material pressure expression is

$$P_{material,shell} = P_{cold\ curve,shell} + P_{ideal\ gas,shell} + P_{artificial\ viscosity}. \tag{14}$$

The ideal gas component treats the shell as an ideal gas of N particles. The thermal energy for an ideal gas, with 3 degrees of freedom, is

$$E_{thermal} = \frac{3}{2}Nk_BT, \tag{15}$$

and the ideal gas equation is

$$P_{ideal\ gas,shell}V_{shell} = N_{particle}k_BT_{shell}. \tag{16}$$

Substitution leads to the shell ideal gas pressure expression

$$P_{ideal\ gas,shell} = \frac{2}{3}\frac{E_{shell}}{V_{shell}}. \tag{17}$$

The "cold curve" pressure term uses the "Birch-Murnaghan form" for finite hydrostatic pressure of cubic materials and is given by

$$P_{cold\ curve,shell} = \frac{3A_1}{2}\left[\left(\frac{\rho_{l,s}}{\rho_{l0}}\right)^{\gamma_1} - \left(\frac{\rho_{l,s}}{\rho_{l0}}\right)^{\gamma_2}\right] \times \left\{1 + \frac{3}{4}\left[A_2 - 4\right]\left[\left(\frac{\rho_{l,s}}{\rho_{l0}}\right)^{2/3} - 1\right]\right\}, \tag{18}$$

where A_1, A_2, γ_1, and γ_2 are "cold curve fitting parameters" dependent on chosen target material [37]. ρ_{l0} is liner density at zero temperature and zero pressure while $\rho_{l,s}$ is the "sth" shell density which changes as interfaces move. The Birch-Murnaghan form is acceptable because the target recovers following compression peak, somewhat suggesting elasticity. Also, target materials such as aluminum are face-centered cubic for the low temperatures and pressures at simulation start. Note that SA doesn't have any simulated structure for the target or lattice coordinates and does not include explicit phase transitions [37], [40].

An artificial viscosity term is present to prevent shells from moving into each other as interfaces are accelerated and decelerated. q_i is based on an arbitrary, integer numerical constant "a." This constant is not analytical but is based on simulation effectiveness towards matching the experiment [37]. The artificial viscosity term is

$$q_i = a^2 \rho_{l,s} (\dot{r}_{i+1} - \dot{r}_i)^2. \tag{19}$$

In addition to PdV work, Planckian blackbody radiation and ohmic heating affect shell thermal energy [37]. These contributions are included through the $\mathcal{P}_{rad}$ and $\mathcal{P}_{\Omega}$ terms. The expression for thermal energy change is simply

$$\dot{E}_{shell} = -\left(\frac{2}{3}\frac{E_{shell}}{V_{shell}} + q_{int}\right)\dot{V}_{shell} + (\mathcal{P}_{\Omega} - \mathcal{P}_{rad}). \tag{20}$$

The radiation loss term is derived from the surface area and the Stefan-Boltzmann law

$$\mathcal{P}_{rad} = \sigma \overline{T}_l^4 \cdot 2\pi r_l \cdot h, \tag{21}$$

where σ is the Stefan-Boltzmann constant. The average liner temperature $\overline{T}_l$ is calculated through

$$\overline{T}_l = \frac{2}{3}\frac{uA\sum_s E_s}{m_l(1+\bar{Z}_l)k_B}, \quad (22)$$

where k_B is the Boltzmann constant, u is the atomic mass unit, and A is the material's atomic mass number. E_s is the shell thermal energy. $\bar{Z}_l$ is average ionization, set at 3 for heated aluminum. m_l is the liner mass. This form for the radiation is justified because of the "optically thick" target and typically lower target temperatures below 100 eV before compression peak [37].

The calculation of ohmic heating is based on induction. Simulation inductance and effective inductance are calculated from geometry while the current is given. Ohmic heating is then

$$\mathcal{P}_\Omega \approx \left|(L_{lc} - L_l)\dot{I}_l I_l - \left(\dot{L}_{lc} - \frac{1}{2}\dot{L}_l\right) I_l^2\right|, \quad (23)$$

where I_l is current at liner surface, $\dot{I}_l$ is the derivative of the current, L_l is the inductance in the magnetic field within the cylinder, and L_{lc} is the effective inductance due to the azimuthal magnetic field. Since the inductance derivative is in time, time derivatives of the innermost and outermost interfaces must be taken as well [37]. The resulting equations are

$$L_{lc}(t) = \frac{\mu_0 h}{2\pi(\beta+1)}\left(1 - \frac{r_g}{r_l}\right), \quad (24)$$

$$\dot{L}_{lc}(t) = \frac{\mu_0 h}{2\pi(\beta+1)}\left(\frac{r_g \dot{r}_l}{r_l^2} - \frac{\dot{r}_g}{r_l}\right), \quad (25)$$

$$L_l(t) = \frac{\mu_0 h(2\beta r_l + r_l + r_g)(r_l - r_g)}{4\pi r_l^2(\beta+1)(2\beta+1)}, \quad (26)$$

and

$$\dot{L}_l(t) = -\frac{\mu_0 h(r_g + \beta r_l)(\dot{r}_g r_l - r_g \dot{r}_l)}{2\pi r_l^3(\beta+1)(2\beta+1)}. \quad (27)$$

C. Code Design and Implementation

The semi-analytical code SA was written in C++. The language is easy to compile, portable, and non-proprietary, unlike MATLAB, IDL, or Mathematica. It is also mid-level and object-oriented, allowing for high performance and extensibility for future modules. The code was compiled and run on commercial PCs using the free Dev-C++ IDE program.

SA solves for velocity and displacement of interfaces between the shells in three steps. First, shell energies and pressures due to magnetic fields and material densities are calculated. Second, differential equations are solved via 1st order Euler's method [41, p. 6]. Third, with velocities in hand, interfaces are then moved. The time is updated and the process restarts. Data is output at specified times in formatted files. There are no meshes or numerical cut-offs unlike more sophisticated codes. Without wide enough shells, failure occurs if the diameter is too short or the current is too high. Calculations use variables stored as 64-bit, floating point numbers.

SA simulates magnetic cylindrical compression of solid rods and allows for scaling of density, pressure, and other experimental parameters. The targets used were Al cylindrical rods of 0.6 to 3 mm diameter. The current pulse approximates the Nevada Terawatt Facility's Zebra pulsed power generator with ~ 100 ns rise time, $\sin^2$ shape, and 1.0 and 1.8 MA current peaks. This is shown by FIG. 16 below. The shape is meant to simulate the current rise and not current behavior after the peak. While 1.0 MA is standard for Zebra, 1.8 MA currents have been obtained using the Load Current Multiplier (LCM) on planar wire array geometry and short circuit experimental configurations [16], [18].

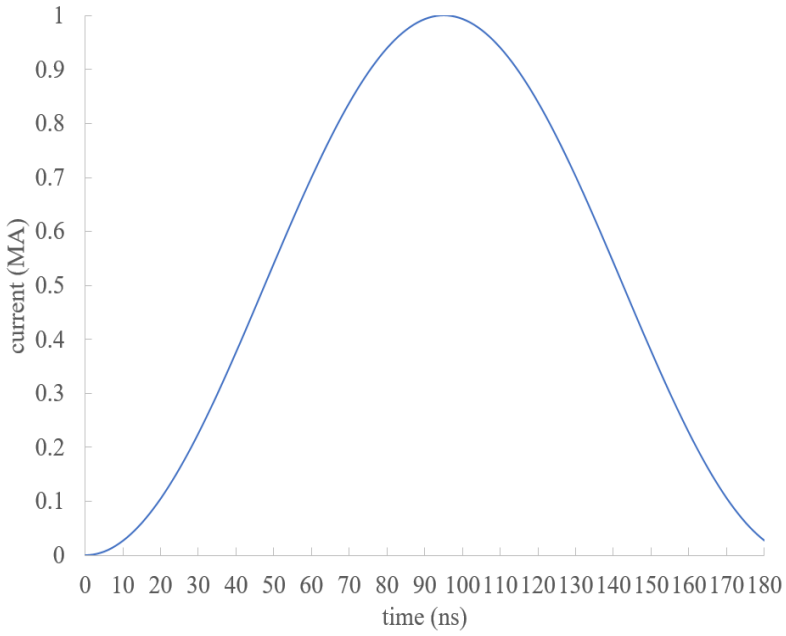

FIG. 16. SA $\sin^2$ current pulse shape with 1.0 MA current peak, 95 ns rise time

IV. SIMULATION RESULTS AND ANALYSIS

The semi-analytic code, called SA, was first benchmarked against one-dimensional radiation magnetohydrodynamic simulations. This is essential to validate the implementation of basic physics in the SA code, enabling us to design magnetically driven cylindrical isentropic compression with an arbitrary current profile. Then a series of simulations with SA were conducted to find the optimum Al rod diameter for designing isentropic compression experiments on the 1.0 MA Zebra pulsed power generator. The simulated parameters of compression and pressure of the Al rods at various diameters were examined. The SA code was applied to experimental designs with the higher current drive of 1.8 MA as well.

A. Comparing SA with MHD codes

Simulations of current driven, magnetic compression of a 1 mm diameter solid Al rod were performed with the 1-D SA code, 1-D MHD code Helios, and 1-D MHD code Mach2. The rod compression used a ~ 95 ns rise time, 1.0 MA peak current.

Helios is a commercial radiation magnetohydrodynamic code and may work in 1-D cylindrical geometry. It calculates fluid material motions of magnetically driven plasma for specified current. The code uses a tabulated equation of state calculated with PROPACEOS and the classical Spitzer function for resistivity [42], [43]. Mach2 is a 1-D or 2-D resistive magnetohydrodynamic code, also solving a complete set of equations with the applied current pulse. It may use the SESAME tabulated equation of state and resistivity database for material dynamics based on cold material calculations or the classical Spitzer function for ionized material [44], [45, pp. 136-143].

FIG. 17 (a) and (b) below show comparisons of Al rod compression as a function of radial distance at 60 and 80 ns. Between the Mach2 simulations with Spitzer resistivity and the SESAME table, the Spitzer model results showed much faster compression wave propagation. The significant difference is attributed to the strong dependence of resistivity on the rod plasma condition, particularly electron temperature. The classical Spitzer resistivity model is based on electron-ion collisions and is proportional to $\sim T_e^{(-3/2)}$. It is valid only at high temperature (> ~ keV) since it assumes a fully ionized plasma. The isentropically compressed Al is expected to have an electron temperature between 1 eV and a few hundred eV. In this T_e regime, the Spitzer model breaks down and an alternative model such as the Lee-More model or a tabulated database is often used [45, pp. 136-143] [46]. Both experimental and numerical determination of temperature-dependent resistivity in the low temperature range is an on-going research area. The comparison of Mach2 simulations to the SA code showed that the semi-analytical code was closest to Mach2 with SESAME resistivity. In contrast, the Helios simulation with the Spitzer model showed no compression and an unphysical, very sharp interface at the outer rod edge. Helios was not compared to SA.

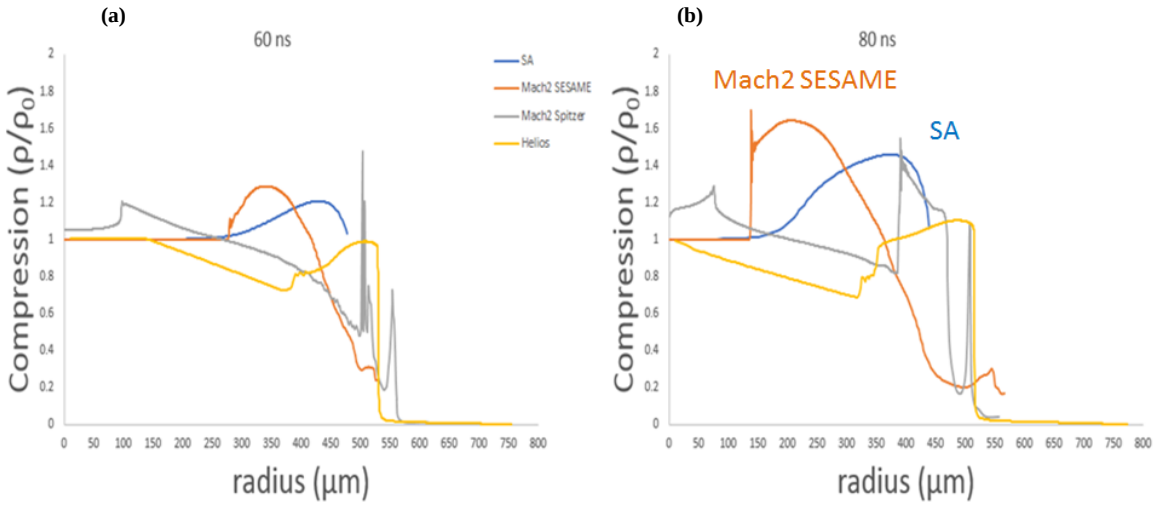

FIG. 17. Compression vs. space for SA, Mach2, and Helios, (a) at 60 ns, (b) at 80 ns. 1.0 MA current peak, ~ 95 ns rise time, 1 mm initial diameter.

The differences in calculations between the SA code and Mach2 SESAME are further investigated. FIG. 18 shows comparisons of maximum magnetic pressure and maximum compression of the interior regions for SA and Mach2 as a function of initial radius at maximum compression time. As FIG. 18 (a) shows, the Mach2 code predicts higher magnetic pressure than SA for initial radii ranging from 300 μm to 800 μm. Since both simulations use the same current pulse, the difference in magnetic pressure is attributed to a combination of diffusion and surface plasma formation. Mach2 calculations include the creation of surface plasma due to ohmic heating, allowing the current to propagate in the conducting plasma at a smaller radius, leading to stronger magnetic pressure.

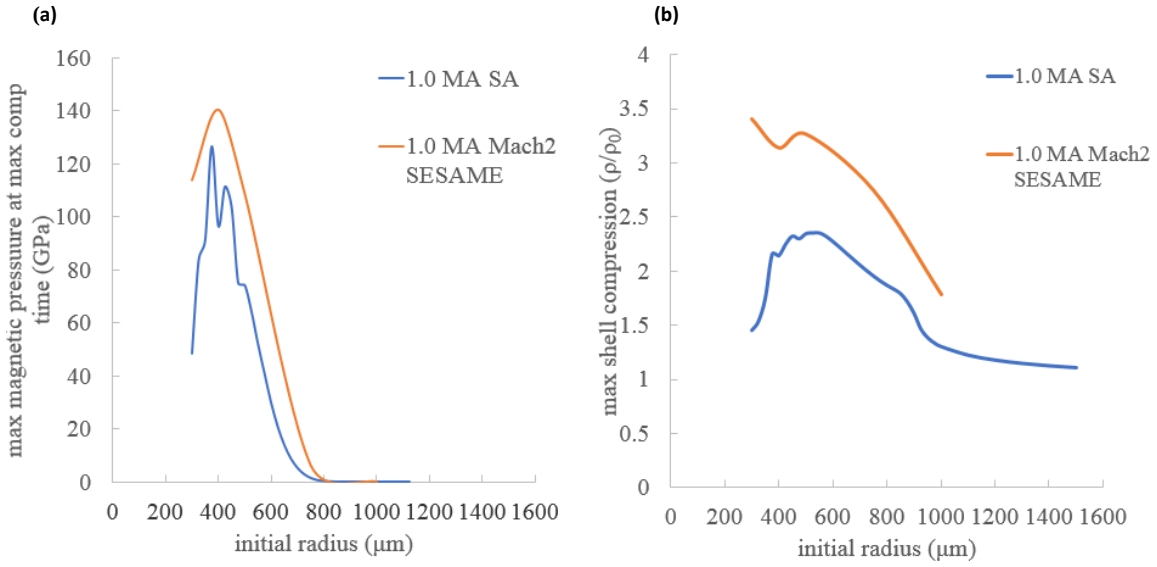

FIG. 18. Max magnetic pressure and maximum compression for SA and Mach2 at max compression time with different initial radii. 1.0 MA current peak, ~ 95 ns rise time.

To address this issue, we tested the provided current with peaks from 1.1 to 1.9 MA to find a current multiplier that would allow SA to achieve closer compression results to Mach2 and on similar timescales. A current multiplier of 1.4 was found. FIG. 19 shows density vs radial space for 1 mm initial diameter, 1.0 MA peak current simulations with SA, Mach2 with SESAME, and a "1.4 MA" SA simulation. By adjusting the current, SA can somewhat better keep up with the Mach2 compression wave. "1.4 MA" SA reaches max compression at about the same time as Mach2.

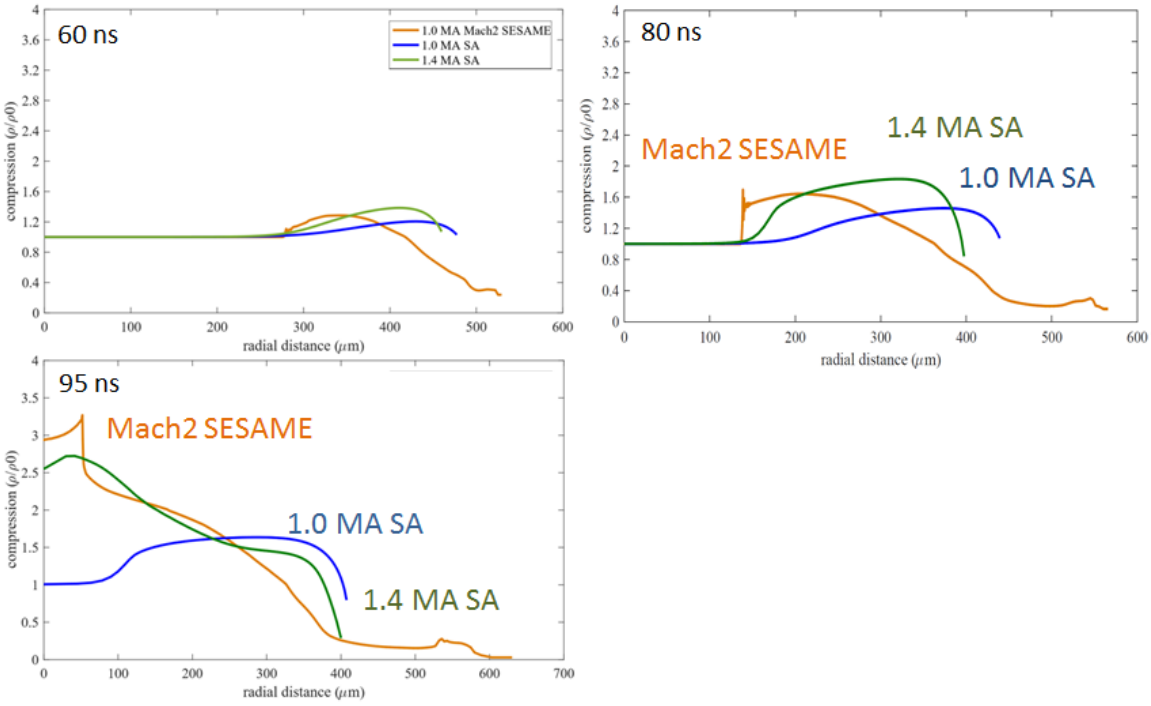

FIG. 19. Compression vs. space for SA, Mach2, (a) 60 ns, (b) 80 ns, (c) 95 ns clockwise from top left. 1.0 MA current peak, ~ 95 ns rise time, 1 mm initial diameter

FIG. 20 shows comparisons of material pressure as a function of radial distance for various times. “1.4 MA SA” is much closer to the Mach2 with SESAME curve than 1.0 MA peak SA, suggesting that SA can roughly follow Mach2 in pressure until near maximum compression time of ~ 95 ns.

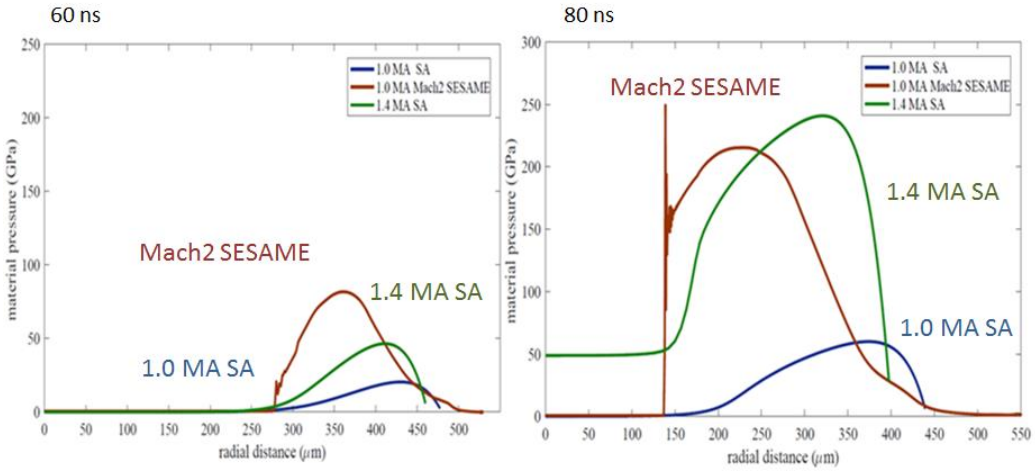

FIG. 20. Pressure vs. space for SA, Mach2, (a) 60 ns, (b) 80 ns left. 1.0 MA current peak, ~ 95 ns rise time, 1 mm initial diameter.

In addition to comparing the compression wave and max compression timing, trial runs from 0.6 to 3.0 mm diameter were conducted with the 1.4 current multiplier. FIG. 21 below shows that 1.4 MA SA gets a larger magnetic pressure at max compression time (a). 1.4 MA SA also gets much closer to Mach2 compressions for rods from 1.6 to 2.0 mm in diameter (b).

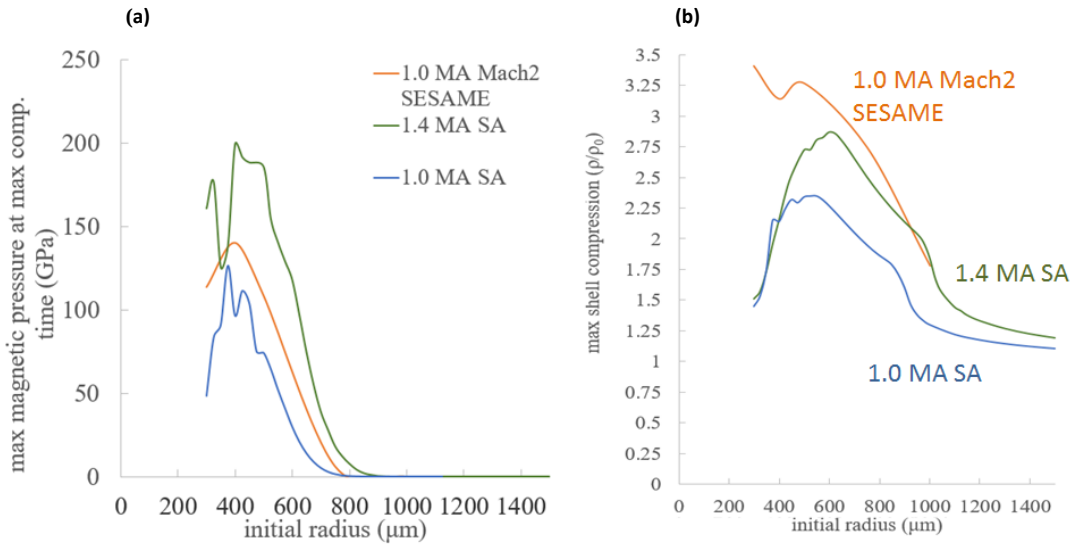

FIG. 21. Max magnetic pressure and max compression at maximum compression time for SA, with and without current multiplier, and Mach2 with different initial radii. 1 mm initial diameter, ~ 95 ns rise time,

B. Simulation of Isentropic, Al Rod Compression with 1.0 MA Pulsed Power Current

Compression and pressure of solid Al rods for various diameters were studied using the SA code with a 1.0 MA, 95 ns rise time pulsed power current. The diameter of the Al rod was varied from 0.6 mm to 3.0 mm. FIG. 22 shows progress of compression propagation in a 1.0 mm diameter rod. The input current continuously increases and peaks at 95 ns. Afterwards the magnetic pressure decreases. The leading edge of the compression reaches the center around 100 ns and keeps compressing to a max of ~ 2.35 at 110 ns.

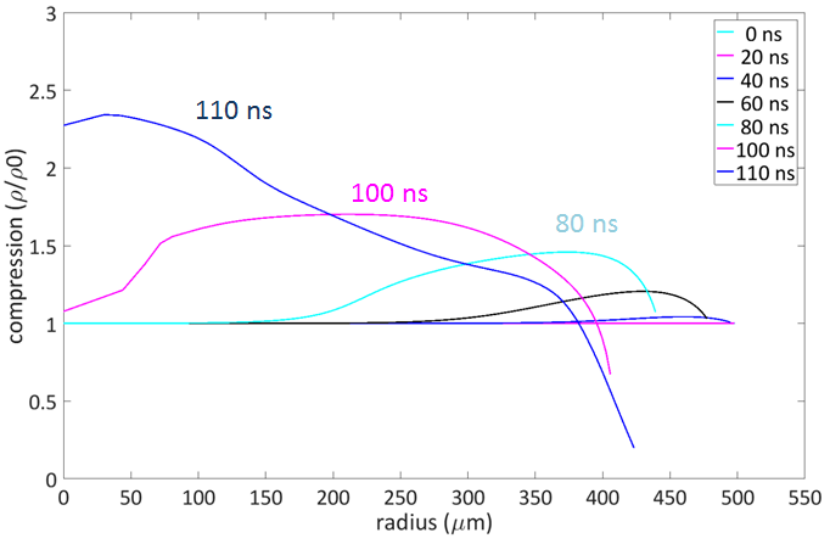

FIG. 22. Compression vs. radial space for 1 mm initial diameter. 1.0 MA current peak, 95 ns rise time.

FIG. 23 below shows the max compression of the Al rod as a function of initial rod radius. For the 1.0 MA current peak and 95 ns rise time, a maximum compression of ~ 2.35 was found for 525 μm (1.05 mm diameter) while compressions of above 1.5 were found within the initial radius range of 400 to 900 μm (0.8 to 1.8 mm diameter). FIG. 23 also shows reduced compression on the far ends of the initial radius range. The magnetic

field pressure for the wider rods was too weak to overcome initial growths in material pressure. For the skinnier rods, stronger magnetic field pressures resulted in compression happening at a faster rate and max compression occurring at lower magnitude due to more rapid growth in material pressure.

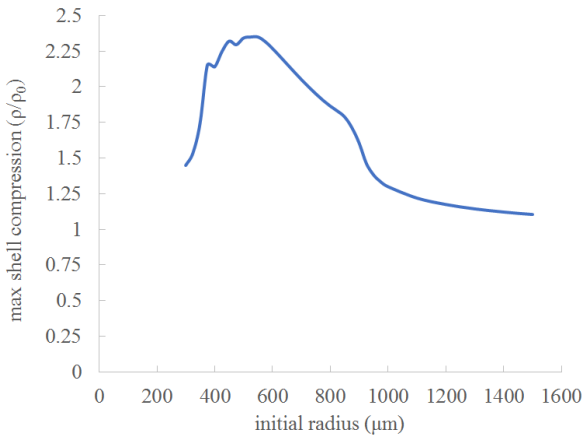

FIG. 23. Max compression shows dependence on initial radius. 1.0 MA current peak, 95 ns rise time.

FIG. 24 (a) and (b) shows compression and pressure profiles of the 525 μm radius Al rod at 116 ns, the max compression time. The rod center within a ~ 100 μm radius is compressed to twice the solid density or higher. From an experimental view, the 200 μm diameter high density plasma is large enough to diagnose with an x-ray radiographic technique. FIG 24 (b) shows that the pressure reaches ~ 1000 GPa at the center. Within the 100 μm radius, the pressure drops from 1000 GPa to 900 GPa, a ~ 10% decrease. Relatively uniform high density Al plasma can be created within this radius for property measurement.

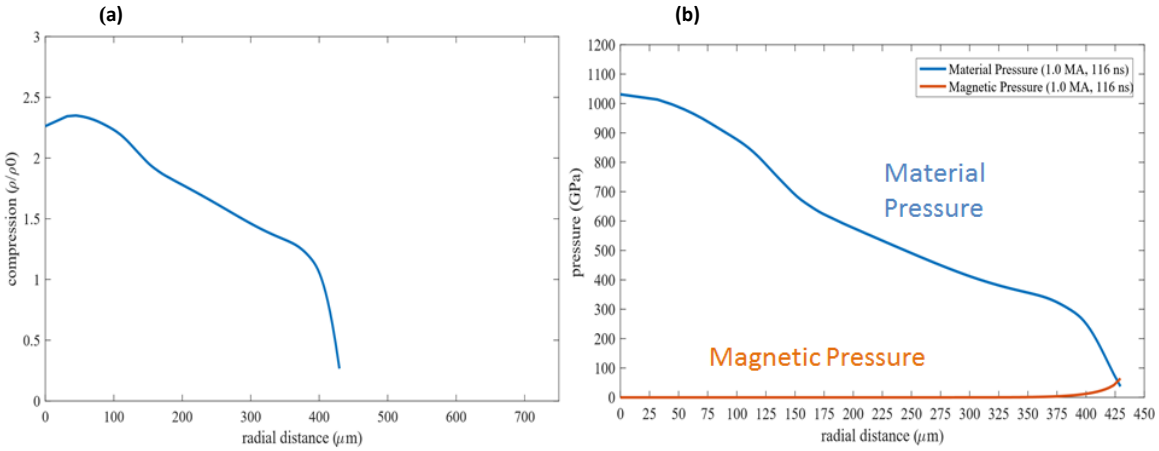

FIG. 24. Compression and pressure over space for 1.05 mm initial diameter at max compression time (116 ns). 1.0 MA current peak, 95 ns rise time

C. Simulation of Isentropic, Al Rod Compression with 1.8 MA Pulsed Power Current

In addition to 1.0 MA, 1.8 MA Zebra style currents were used to study the compression. While Zebra is mainly operated with 1.0 MA current, higher currents are possible with the load current multiplier (LCM) and short circuit load types [16], [18]. With this configuration, the current peak is increased by 80% while the rise time is maintained with a 95 ns peak. The faster rise of the 1.8 MA current pulse compresses an Al rod more rapidly than the 1.0 MA drive and allows us to study a wider range of conditions. The use of higher current tends to increase the maximum compression and maximum material pressures. FIG. 25 shows a comparison of Al rod compression with 1.0 and 1.8 MA current drives as a function of initial rod radius. With 1.8 MA, 650 μm (1.3 mm diameter) offers the most compression with 3.32. A compression of 2 is found for initial radii from 400 μm to 1100 μm (0.8 to 2.2 mm initial diameter).

Compression for rods skinner than 425 μm is still limited and may in fact be less than for 1.0 MA. The rapid current rise already prevented much compression with the 1.0 MA current and it is only faster with 1.8 MA. A longer current pulse may be necessary.

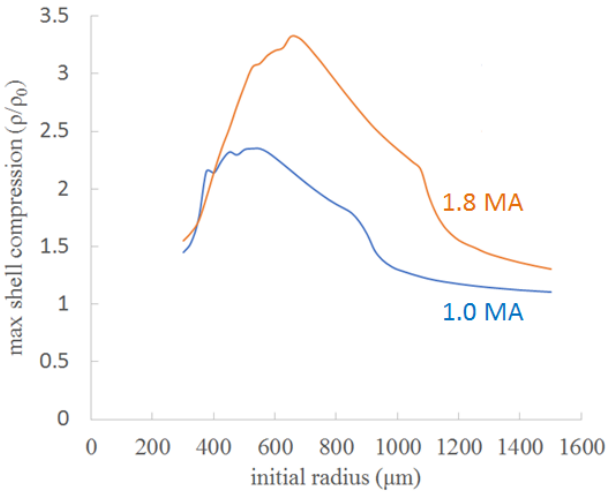

FIG. 25. Comparison of max compression for 1.0 and 1.8 MA current peaks, 95 ns rise time pulses

In FIG. 26 the internal density and pressure at the compression stagnation time for the optimum 650 μm initial radius (1.3 mm diameter) are shown. The Al is compressed more than 3 times higher than solid density, with a compression variation of ~ 8% over ~ 150 μm from the center. The maximum material pressure is simulated to be ~ 3600 GPa at rod center. This is a significant increase in the pressure (~ 3.6 times higher) by increasing the peak current by 1.8 times. The results show the upper limit of the high energy density Al plasma conditions that can be achieved by the pulsed power capability of Zebra. With different pulse configurations and choices of various rod diameters, aluminum states in a wide range of compression and pressure domains can be investigated at the NTF.

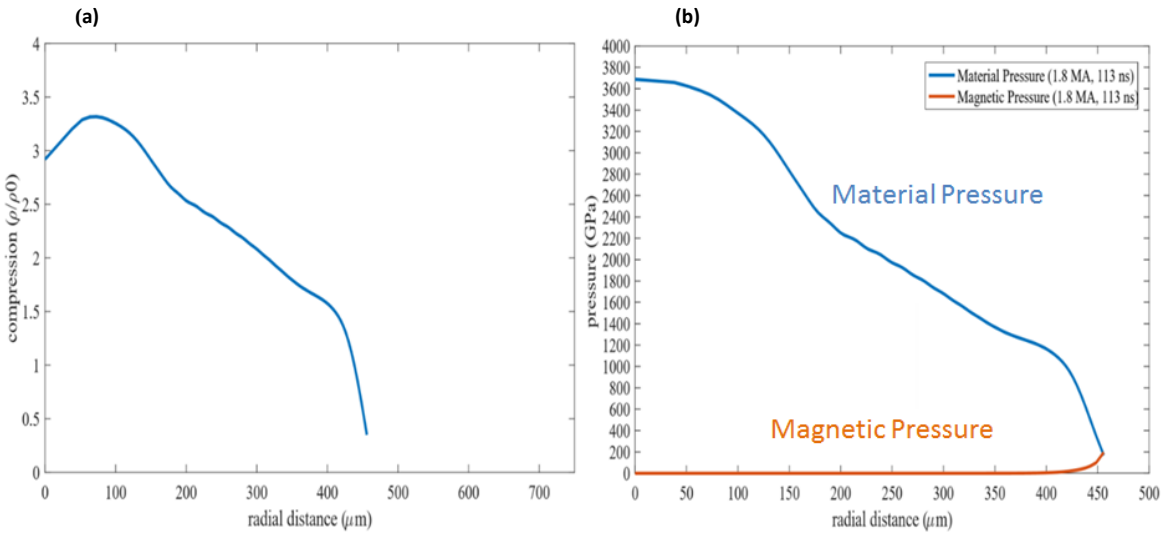

FIG. 26. Compression and pressure over space for 1.3 mm initial diameter at max compression time (113 ns). 1.8 MA current peak, 95 ns rise time

D. SA Code Limitations

SA has several limitations. The code does not model current diffusion into the rod though the magnetic field is present into interior shells. There is no conduction or material transport between the discrete shells. No inner "zero radius" boundary condition is maintained. There is also no outer boundary condition or stress/strain mechanism, so material expanding outward may do so until the pressures dramatically decrease from the expansion. SA does not accurately simulate after max compression. Radiation is simplified to only a cooling mechanism and no opacity is incorporated. Lastly, since the semi-analytical model is only 1-D, it cannot simulate the Rayleigh-Taylor instabilities. These are present between layers of differing density being compressed by an external pressure, such as gravity. FIG. 27 shows a hydrodynamic simulation with heavy fluid sitting on top of fluid with lesser density. Instability flutes form and then turbulence [10, p. 131]. Because of the lack of these 2-D effects, densities and pressures at the surface were not physical.

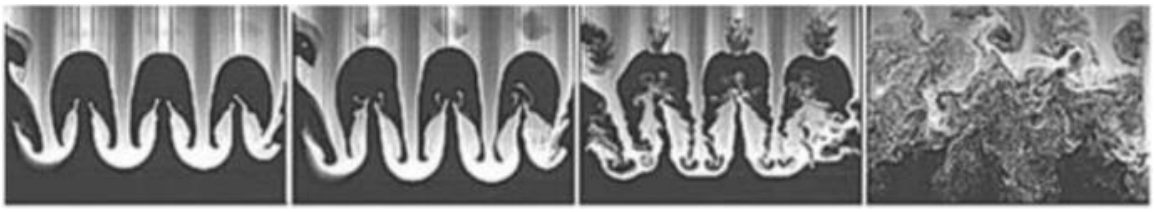

FIG. 27. Rayleigh-Taylor hydrodynamic simulation results with heavy fluid sitting atop fluid with lesser density. Gravitational force results in instability flutes leading to turbulence. Time passes going left to right [10, p. 131].

Continued work on SA requires experiments and development of additional modules. A semi-analytical code is dependent on constants, since computational work is kept simple for quick run time. Experiments must provide information on density, pressure, and temperature. Then, numerical constants may be altered to match experimental results.

SA should also be upgraded with new modules staying within the code's philosophy. Currently, ionization is held at room temperature level. If effective ablation rates can be found and scaled to experimental results, it may be possible to simply model plasma creation. Finally, the differential equations could be solved with higher order Euler's methods [41].

V. CONCLUSIONS

Magnetically driven cylindrical compression of solid aluminum rods has been numerically studied. Based on a semi-analytical model developed for Magnetized Liner Inertial Fusion (MagLIF), a 1-D code called SA has been written to design a cylindrical isentropic compression experiment for the Zebra pulsed power generator at the Nevada Terawatt Facility. In SA, simplified magnetic and material pressures acting on and within the cylinder are calculated using a current pulse, simulation geometry, and numerical constants. SA enables the experimental and target parameters to be explored.

To test the physics within the code, the SA calculation for a magnetically driven 1.0 mm diameter aluminum rod was compared with 1-D magnetohydrodynamic code Mach2, with SEASAME data tables or the classical Spitzer function. The Mach2 simulations with these two resistivity models showed significant differences in the speed of the compression wave and spatial compression. The SA calculation was found to be closer to Mach2 with SESAME, suggesting the numerical parameters in SA mimic the resistivity of isentropically compressed aluminum in the range of a few to several hundred GPa. The magnetic pressure produced in SA is weaker than for Mach2 with the same input current pulse. This could be attributed to changes in current distribution and surface plasma formation by ablation included in the Mach2 code. It is found that the material pressure and compression produced in Mach2 can be approximately reproduced with SA using a numerical multiplier of ~ 1.4 for the current pulse peak.

The SA code was used to simulate compression of aluminum rod diameters using 95 ns rise time, 1.0 MA and 1.8 MA peak current pulses. The rod diameters were varied from 0.6 mm to 3.0 mm to find the optimum size for maximum compression. With 1.0

MA current, an optimum diameter of 1.05 mm was found with a maximum compression of ~ 2.35 and pressure of ~ 900 GPa or higher within an inner radial space of 100 μm. The higher peak current of 1.8 MA shifts the optimum diameter to 1.30 mm, with a compression of ~ 3.32 and a peak pressure of nearly 3.4 TPa or higher within the same radius. Simulation results with the Zebra current show the internal pressure of magnetically compressed Al rods in the cylindrical geometry can be significantly higher than for planar isentropic compression experiments that were performed in the past. This is most likely because the peak pressure reached is due in part to non-isentropic compression with heating also present in SA. The pressure and compression results are accurate enough for experimental use because they are matching within an order of magnitude the pressure and compression from Mach2 SESAME. A campaign using the Zebra pulsed power generator would allow SA to be made more accurate through adjusting of numerical constants.

APPENDIX I. SA SIMULATION SET-UPS

Various numerical and SI constants, published by McBride and Slutz with their semi-analytical model, were used in SA simulations [37]. Here A is the atomic weight. A1 and A2 are numerical constants used in the cold curve, Birch-Murnaghan form for aluminum material. h is the height of the rod used in the interface ordinary differential equations. I_0 is the peak current occurring at the end of the rise time. $rhol_0$ is the initial density. Sim Time is the amount of time simulated. Time Between Output is the time between output lines in data files. If this is 1 ns, every line in the output files takes place at one more nanosecond in time. Shells is the number of divisions that the solid cylinder is broken into. aq is a numerical constant for the artificial viscosity. McBride recommended 1 - 3 for this constant. rg is the first interface. To avoid numerical errors, this cannot be zero. Zavgl is the average ionization, not changed in the SA code over the course of the simulation. This is used in the average temperature calculation for Planckian radiation.

Table. I. SA Simulation Parameters

	1.0 MA, 95 ns peak	**"1.4 MA," 95 ns peak**	**1.8 MA, 95 ns peak**
A	26.98	26.98	26.98
A1	76×10^9	76×10^9	76×10^9
A2	3.9	3.9	3.9
h (m)	0.01	0.01	0.01
I_0 (A)	1.0×10^6	1.4×10^6	1.8×10^6
$rhol_0$ (kg/m^3)	2700	2700	2700
Sim Time (ns)	180	180	180
Time Between Output (ns)	1	1	1
Shells	120	110	100
aq	3	3	3
rg (m)	5E-9	5E-9	5E-9
Zavgl	3	3	3

APPENDIX II. COMPARISON OF SA AND MACH2 RUN TIMES

Simulations of 1.0 MA current pulses with 1 mm diameter cylinder targets were conducted by 1-D SA and Mach2, with the latter utilizing SESAME table resistivity. The simulation time and number of timesteps were similar, specifically 180 ns and 18000 time steps. The speed of SA was dependent on the number of shells used, which determined the amount of differential equations solved. With 100 shells, SA took approximately 60 s. 335 shells was the most allowed without failure for the given current and diameter. This amount of shells increased the time needed to ~ 180 s. The SA simulations were done by a single CPU with the Windows7 operating system. By comparison, Mach2 with 500 spatial cells completed a trial in 256 seconds, with a single CPU in a Linux environment. These results suggest that the time-saving benefit of using a 1-D semi-analytical model is small when compared to using optimized 1-D MHD code in an efficient environment [47].

REFERENCES

[1] A. Jayaraman, "Diamond anvil cell and high-pressure physical investigations," *Review of Modern Physics,* vol. 55, no. 65, pp. 65-108, 1983.

[2] H. Mao and R. J. Hemley, "Ultrahigh-pressure transitions in solid hydrogen," *Review of Modern Physics,* vol. 66, no. 2, pp. 671-692, 1994.

[3] M. D. Knudson, D. L. Hanson, J. E. Bailey, C. A. Hall, J. R. Asay and W. W. Anderson, "Equation of State Measurements in Liquid Deuterium to 70 GPa," *Physical Review Letters,* vol. 87, no. 22, p. 225501, 2001.

[4] O. A. Hurricane, D. A. Callahan, D. T. Casey, P. M. Celliers, C. Cerjan, E. L. Dewald, T. R. Dittrich, T. Döppner, D. E. Hinkel, L. F. Berzak Hopkins, J. L. Kline, S. Le Pape, T. Ma, A. G. MacPhee, J. L. Milovich, A. Pak, H.-S. Park, P. K. Patel, B. A. Remington, J. D. Salmonson, P. T. Springer and R. Tommasini, "Fuel gain exceeding unity in an inertially confined fusion implosion," *Nature Letters,* vol. 506, no. 7488, pp. 343-348, 2014.

[5] J. Lindl, "Development of the indirect-drive approach to inertial confinement fusion and the target physics basis for ignition and gain," *Physics of Plasmas,* vol. 2, no. 11, pp. 3933-4024, 1995.

[6] C. A. Hall, "Isentropic compression experiments on the Sandia Z accelerator," *Physics of Plasmas,* vol. 7, no. 5, pp. 2069-2075, 2000.

[7] J.-P. Davis, "Experimental measurement of the principal isentrope for aluminum 6061-T6 to," *Journal of Applied Physics,* vol. 99, no. 10, p. 103512, 2006.

[8] J. Eggert, R. Smith, D. Swift, R. Rudd, D. Fratanduono, D. Braun, J. Hawreliak, J. McNaney and G. Collins, "Ramp compression of tantalum to 330 GPa," *High Pressure Research,* vol. 35, no. 4, pp. 339-354, 2015.

[9] M. R. Martin, R. W. Lemke, R. D. McBride, J. P. Davis, D. H. Dolan, M. D. Knudson, K. R. Cochrane, D. B. Sinars, I. C. Smith, M. Savage, W. A. Stygar, K. Killebrew, D. G. Flicker and M. C. Herrmann, "Solid liner implosions on Z for producing multi-megabar, shockless compressions," *Physics of Plasmas,* vol. 19, no. 5, p. 056310, 2012.

[10] S. Pfalzner, An Introduction to Inertial Confinement Fusion, New York : Taylor & Francis Group, LLC, 2006 .

[11] P. O. K. Krehl, "The classical Rankine-Hugoniot jump conditions, an important cornerstone of modern shock wave physics: ideal assumptions vs. reality," *The European Physical Journal H,* vol. 40, no. 2, pp. 159-204, 2015.

[12] C. J. Pickard and R. J. Needs, "Aluminium at terapascal pressures," *Nature Materials* , vol. 9, pp. 624-627, 2010.

[13] K. Lorenz, M. Edwards, A. Jankowski, S. Pollaine, R. Smith and B. Remington, "High pressure, quasi-isentropic compression experiments on the Omega laser," *High Energy Density Physics,* vol. 2, no. 3-4, pp. 113-125, 2006.

[14] D. C. Swift and R. P. Johnson, "Quasi-isentropic compression by ablative laser loading: Response of materials to dynamic loading on nanosecond time scales," *Physical Review E,* vol. 71, no. 6, p. 066401, 2005.

[15] S. Fuelling, T. J. Awe, B. S. Bauer, T. Goodrich, A. Haboub, V. V. Ivanov, V. Makhin, A. Oxner, R. Presura and R. E. Siemon, "A Zebra Experiment to Study Plasma Formation by Megagauss Fields," *IEEE Transactions on Plasma Science,* vol. 36, no. 1, pp. 62-69, 2008.

[16] A. S. Safronova, V. L. Kantsyrev, M. E. Weller, V. V. Shlyaptseva, I. K. Shrestha, A. Stafford, M. T. Schmidt-Petersen, M. Y. Lorance, K. A. Schultz and A. S. Chuvatin, "Larger sized planar wire arrays of complex configuration on 1.5–1.8 MA Z-pinch," *Physics of Plasmas,* vol. 23, no. 10, p. 101210, 2016.

[17] M. E. Cuneo, M. C. Herrmann, D. B. Sinars, S. A. Slutz, W. A. Stygar, R. A. Vesey, A. B. Sefkow, G. A. Rochau, G. A. Chandler, J. E. Bailey, J. L. Porter, R. D. McBride, D. C. Rovang, M. G. Mazarakis, E. P. Yu, D. C. Lamppa, K. J. Peterson, C. Nakhleh, S. B. Hansen, A. J. Lopez, M. E. Savage, C. A. Jennings, M. R. Martin, R. W. Lemke, B. W. Atherton, I. C. Smith, P. K. Rambo, M. Jones, M. R. Lopez, P. J. Christenson, M. A. Sweeney, B. Jones, L. A. McPherson, E. Harding, M. R. Gomez, P. F. Knapp, T. J. Awe, R. J. Leeper, C. L. Ruiz, G. W. Cooper, K. D. Hahn, J. McKenney, A. C. Owen, G. R. McKee, G. T. Leifeste, D. J. Ampleford, E. M. Waisman, A. Harvey-Thompson, R. J. Kaye, M. H. Hess, S. E. Rosenthal and M. K. Matzen, "Magnetically Driven Implosions for Inertial Confinement Fusion at Sandia National Laboratories," *IEEE Transactions on Plasma Science,* vol. 40, no. 12, pp. 3222-3245, 2012.

[18] A. S. Chuvatin, V. L. Kantsyrev, L. I. Rudakov, M. E. Cuneo, A. L. Astanovitskiy, R. Presura, A. S. Safronova, W. Cline, K. M. Williamson, I. Shrestha, G. C. Osborne, B. LeGalloudec, V. Nalajala, T. D. Pointon and K. A. Mikkelson, "Operation of a load current multiplier on a nanosecond mega-ampere pulse

forming line generator," *Physical Review ST Accelerators and Beams,* vol. 13, no. 1, p. 010401, 2010.

[19] M. K. Matzen, M. A. Sweeney, R. G. Adams, J. R. Asay, J. E. Bailey, G. R. Bennett, D. E. Bliss, D. D. Bloomquist, T. A. Brunner, R. B. Campbell, G. A. Chandler, C. A. Coverdale, M. E. Cuneo, J.-P. Davis, C. Deeney, M. P. Desjarlais, G. L. Donovan, C. J. Garasi, T. A. Haill, C. A. Hall, D. L. Hanson, M. J. Hurst, B. Jones, M. D. Knudson, R. J. Leeper, R. W. Lemke, M. G. Mazarakis, D. H. McDaniel, T. A. Mehlhorn, T. J. Nash, C. L. Olson, J. L. Porter, P. K. Rambo, S. E. Rosenthal, G. A. Rochau, L. E. Ruggles, C. L. Ruiz, T. W. L. Sanford, J. F. Seamen, D. B. Sinars, S. A. Slutz, I. C. Smith, K. W. Struve, W. A. Stygar, R. A. Vesey, E. A. Weinbrecht, D. F. Wenger and E. P. Yu, "Pulsed-power-driven high energy density physics and inertial confinement fusion research," *Physics of Plasmas,* vol. 12, no. 5, p. 055503, 2005.

[20] T. J. Awe, B. S. Bauer, S. Fuelling and R. E. Siemon, "The Evolving Structure of Plasma Formed From the Surface of Aluminum Rods Driven to Megaampere Current," *IEE Transactions on Plasma Science,* vol. 39, no. 11, pp. 2418-2419, 2011.

[21] K. J. Peterson, D. B. Sinars, E. P. Yu, M. C. Herrmann, M. E. Cuneo, S. A. Slutz, I. C. Smith, B. W. Atherton, M. D. Knudson and C. Nakhleh, "Electrothermal instability growth in magnetically driven pulsed power liners," *Physics of Plasmas,* vol. 19, no. 9, p. 92701, 2012.

[22] H. Sawada, Y. Sentoku, A. Bass, B. Griffin, R. Pandit, F. Beg, H. Chen, H. McLean, A. J. Link and P. K. Patel, "Characterization of intense laser-produced fast electrons using hard x-rays via bremsstrahlung," *Journal of Physics B: Atomic, Molecular and Optical Physics,* vol. 48, no. 22, p. 224008, 2015.

[23] T. A. Shelkovenko, D. B. Sinars, S. A. Pikuz, K. M. Chandler and D. A. Hammer, "Point-projection x-ray radiography using an X pinch as the radiation source," *Review of Scientific Instruments,* vol. 72, no. 1, pp. 667-670, 2001.

[24] B. R. Maddox, H. S. Park, B. A. Remington, C. Chen, S. Chen, S. T. Prisbrey, A. Comley, C. A. Back, C. Szabo, J. F. Seely, U. Feldman, L. T. Hudson, S. Seltzer, M. J. Haugh and Z. Ali, "Absolute measurements of x-ray backlighter sources at energies above 10 keV," *Physics of Plasmas,* vol. 18, no. 5, p. 056709, 2011.

[25] D. H. Kalantar, J. F. Belak, G. W. Collins, J. D. Colvin, H. M. Davies, J. H. Eggert, T. C. Germann, J. Hawreliak, B. L. Holian, K. Kadau, P. S. Lomdahl, H. E. Lorenzana, M. A. Meyers, K. Rosolankova, M. S. Schneider, J. Sheppard, J. S. Stölken and J. S. Wark, "Direct Observation of the alpha - epsilon Transition in

Shock-Compressed Iron via Nanosecond X-Ray Diffraction," *Physical Review Letters,* vol. 95, no. 7, p. 075502, 2005.

[26] R. Tommasini, S. P. Hatchett, D. S. Hey, C. Iglesias, N. Izumi, J. A. Koch, O. L. Landen, A. J. MacKinnon, C. Sorce, J. A. Delettrez, V. Y. Glebov, T. C. Sangster and C. Stoeckl, "Development of Compton radiography of inertial confinement fusion implosions," *Physics of Plasmas,* vol. 18, no. 5, p. 056309, 2011.

[27] S. Glenzer and R. Redmer, "X-ray Thomson scattering in high energy density plasmas," *Reviews of Modern Physics,* vol. 81, no. 4, pp. 1625-1663, 2009.

[28] V. E. Fortov, R. I. Ilkaev, V. A. Arinin, V. V. Burtzev, V. A. Golubev, I. L. Iosilevskiy, V. V. Khrustalev, A. L. Mikhailov, M. A. Mochalov, V. Y. Ternovoi and M. V. Zhernokletov, "Phase Transition in a Strongly Nonideal Deuterium Plasma Generated by Quasi-Isentropical Compression at Megabar Pressures," *Physical Review Letters,* vol. 99, no. 18, p. 185001, 2007.

[29] G. V. Boriskov, A. I. Bykov, N. I. Egorov, M. I. Dolotenko, V. N. Pavlov and V. I. Timareva, "Isentropic Compression of Substances Using Ultra-High Magnetic Field: Zero Isotherms of Protium and Deuterium in Pressure Range up to ~5 Mbar," *Contrib. to Plasma Phys,* vol. 51, no. 4, pp. 339-348, 2010.

[30] I. Lomonosov, "Multi-phase equation of state for aluminum," *Laser Particle Beams,* vol. 25, no. 4, pp. 567-584, 2007.

[31] A. S. Vladimirov, N. P. Voloshin, V. N. Nogin, A. V. Petrovtsev and V. A. Simonenko, "Shock compressibility of aluminum at p > 1 Gbar," *Sov. Phys. JETP Lett.,* vol. 39, no. 2, pp. 82-84, 1984.

[32] O. Mikhailova, M. A. Mochalov, A. I. Sokolova and V. D. Urlin, "Quasi-Isentropic Compression of Liquid Xenon to a Density of 20 g/cm^3 at a Pressure of ~720 GPa," *High. Temp.,* vol. 38, no. 2, pp. 210-214, 2000.

[33] A. I. Pavlovski, G. D. Kuleshov, G. V. Sklizkov, Y. A. Zusin and A. I. Gerasimo, "High-current iron-free betatron," *Soviet Physics Doklady,* vol. 10, no. 1, pp. 30-32, 1965.

[34] T. J. Awe, B. S. Bauer, S. Fuelling and R. E. Siemon, "Threshold for Thermal Ionization of an Aluminum Surface by Pulsed Megagauss Magnetic Field," *Physical Review Letters,* vol. 104, no. 3, p. 035001, 2010.

[35] T. J. Awe, B. S. Bauer, S. Fuelling, I. R. Lindemuth and R. E. Siemon, "Experimental investigation of thermal plasma formation from thick aluminum

surfaces by pulsed multimegagauss magnetic field," *Physics of Plasmas,* vol. 17, no. 10, p. 102507, 2010.

[36] T. J. Awe, B. S. Bauer, S. Fuelling and R. E. Siemon, "Mitigation of nonthermal plasma production to measure the pulsed magnetic field threshold for the thermal formation of plasma from thick aluminum surfaces," *Physics of Plasmas,* vol. 18, no. 5, p. 056304, 2011.

[37] R. McBride and S. Slutz, "A semi-analytic model of magnetized liner inertial fusion," *Physics of Plasmas,* vol. 22, no. 5, p. 052708, 2015.

[38] S. A. Slutz, M. C. Herrmann, R. A. Vesey, A. B. Sefkow, D. B. Sinars, D. C. Rovang, K. J. Peterson and M. E. Cuneo, "Pulsed-power-driven cylindrical liner implosions of laser preheated fuel magnetized with an axial field," *Physics of Plasmas,* vol. 17, no. 5, p. 056303, 2010.

[39] M.R. Gomez, S.A. Slutz, A.B. Sefkow, D.B. Sinars, K.D. Hahn, S.B. Hansen, E.C. Harding, P.F. Knapp, P.F. Schmit, C.A. Jennings, T.J. Awe, M. Geissel, D.C. Rovang, G.A. Chandler, G.W. Cooper, M.E. Cuneo, A.J. Harvey-Thompson, M.C. Herrmann, M.H. Hess, O. Johns, D.C. Lamppa, M.R. Martin, R.D. McBride, K.J. Peterson, J.L. Porter, G.K. Robertson, G.A. Rochau, C.L. Ruiz, M.E. Savage, I.C. Smith, W.A. Stygar and R.A. Vesey, "Experimental Demonstration of Fusion-Relevant Conditions in Magnetized Liner Inertial Fusion," *Physical Review Letters,* vol. 113, no. 15, p. 155003, 2014.

[40] F. Birch, "Finite Elastic Strain of Cubic Crystals," *Physical Review,* vol. 71, no. 11, pp. 809-824, 1947.

[41] T. M. Shih, Numerical Heat Transfer, New York: Hemisphere Publishing Corporation, 1984.

[42] J. McFarlane, I. E. Golovkin and P. Woodruff, "HELIOS-CR – A 1-D radiation-magnetohydrodynamics code with inline atomic kinetics modeling," *Journal of Quantitative Spectroscopy and Radiative Transfer,* vol. 99, no. 1-3, pp. 381-397, 2006.

[43] S. S. Harilal, J. J. MacFarlane, I. E. Golovkin, P. R. Woodruff and P. Wang, "Modeling of EUV emission and conversion efficiency from laser-produced tin plasmas for nanolithography", *Proc. SPIE* 6921, Emerging Lithographic Technologies XII, 692133, 2008.

[44] H. U. Rahman, F. J. Wessel, P. Ney, R. Presura, R. Ellahi and P. K. Shukla, "Shock waves in a Z-pinch and the formation of high energy density plasma," *Physics of Plasmas*, vol. 19, no. 12, p. 122701, 2012.

[45] L. Spitzer, Physics of Fully Ionized Gases, New York : John Wiley & Sons , 1962.

[46] Y. T. Lee and R. M. More, "An electron conductivity model for dense plasmas," *Physics of Fluids*, vol. 27, no. 5, pp. 1273-1286, 1984.

[47] J. Narkis, personal communication, April 2017.